Twofold Anisotropic Superconductivity in Bilayer T_d-$MoTe_2$

Zizhong Li,[1,*] Apoorv Jindal,[2,*] Alex Strasser,[3] Yangchen He,[1] Wenkai Zheng,[4,5] David Graf,[5] Takashi Taniguchi,[6] Kenji Watanabe,[6] Luis Balicas,[5] Cory R. Dean,[2] Xiaofeng Qian,[3,†] Abhay N. Pasupathy,[2,‡] and Daniel A. Rhodes[1,§]

[1]*Department of Materials Science and Engineering, University of Wisconsin-Madison, Madison, Wisconsin 53706, USA*
[2]*Department of Physics, Columbia University, New York, New York 10027, USA*
[3]*Department of Materials Science and Engineering, Texas A&M University, College Station, Texas 77843, USA*
[4]*Department of Physics, Florida State University, Tallahassee, Florida 32306, USA*
[5]*National High Magnetic Field Laboratory, Tallahassee, Florida 32310, USA*
[6]*National Institute for Materials Science, Tsukuba, Japan*

(Received 28 April 2024; accepted 10 September 2024; published 22 November 2024)

Noncentrosymmetric two-dimensional superconductors with large spin-orbit coupling offer an opportunity to explore superconducting behaviors far beyond the Pauli limit. One such superconductor, few-layer T_d-$MoTe_2$, has large upper critical fields that can exceed the Pauli limit by up to 600%. However, the mechanisms governing this enhancement are still under debate, with theory pointing toward either spin-orbit parity coupling or tilted Ising spin-orbit coupling. Moreover, ferroelectricity concomitant with superconductivity has been recently observed in the bilayer, where strong changes to superconductivity can be observed throughout the ferroelectric transition pathway. Here, we report the superconducting behavior of bilayer T_d-$MoTe_2$ under an in-plane magnetic field, while systematically varying magnetic field angle and out-of-plane electric field strength. We find that superconductivity in bilayer $MoTe_2$ exhibits a twofold symmetry with an upper critical field maxima occurring along the b axis and minima along the a axis. The twofold rotational symmetry remains robust throughout the entire superconducting region and ferroelectric hysteresis loop. Our experimental observations of the spin-orbit coupling strength (up to 16.4 meV) agree with the spin texture and spin splitting from first-principles calculations, indicating that tilted Ising spin-orbit coupling is the dominant underlying mechanism.

DOI: 10.1103/PhysRevLett.133.216002

In recent years, many two-dimensional (2D) superconductors (SCs) have been shown to substantially exceed the Pauli limit (H_p). However, the primary mechanisms governing these enhancements are difficult to assign, as many different mechanisms are possible, including Ising spin-orbit coupling (SOC) types I (intervalley [1–3]) and II (interorbital [4–6]), tilted Ising SOC [7,8], dynamic spin-momentum locking [9], as well as the recently proposed spin-orbit parity coupling (SOPC) [10,11]. For few-layer $MoTe_2$, evidence for either SOPC [10] or tilted Ising SOC has been reported [7,8]. Both mechanisms can enhance the in-plane upper critical fields up to several times of H_p and follow the same Ginzburg-Landau square-root-dependence on temperature. However, the lack of accurate in-plane angle-dependent measurements on pristine samples with a nearly intrinsic Fermi level leaves open the question as to which mechanism is dominant. For SOPC to lock spins and enhance the upper critical field there must exist strong orbital pair mixing near the Fermi level. In few-layer WTe_2 and $MoTe_2$, this is realized through band inversion which also enables topological edge states [12,13]. For tilted Ising SOC, spins are locked by strong spin-orbit coupling enabled by broken inversion symmetry. Without disorder, the enhancement of upper critical fields via SOPC (max $\sim 2.5H_p$ for the 1T′ structure) is generally weaker than the enhancement by tilted Ising SOC. As a result, the differences between the two mechanisms can be discerned by mapping the enhancement of H_{c2} and its anisotropy along in-plane directions. Understanding the underlying mechanism responsible for enhanced upper critical fields is important for exploring unconventional states in 2D SCs. This is particularly true for exploring finite momentum states [14–18] that exceed H_p and establish a Fulde-Ferrell-Larkin-Ovchinnikov (FFLO) state and for determining potential candidates for topological superconductivity. In this Letter we provide insight on the mechanism that governs the enhanced upper critical fields and the nontrivial superconducting properties of bilayer T_d-$MoTe_2$ by examining the interplay between SOC and superconductivity. This is achieved by a systematic exploration of the effects of

*These two authors contributed equally.
†Contact author: feng@tamu.edu
‡Contact author: apn2108@columbia.edu
§Contact author: darhodes@wisc.edu

 © 2024 American Physical Society

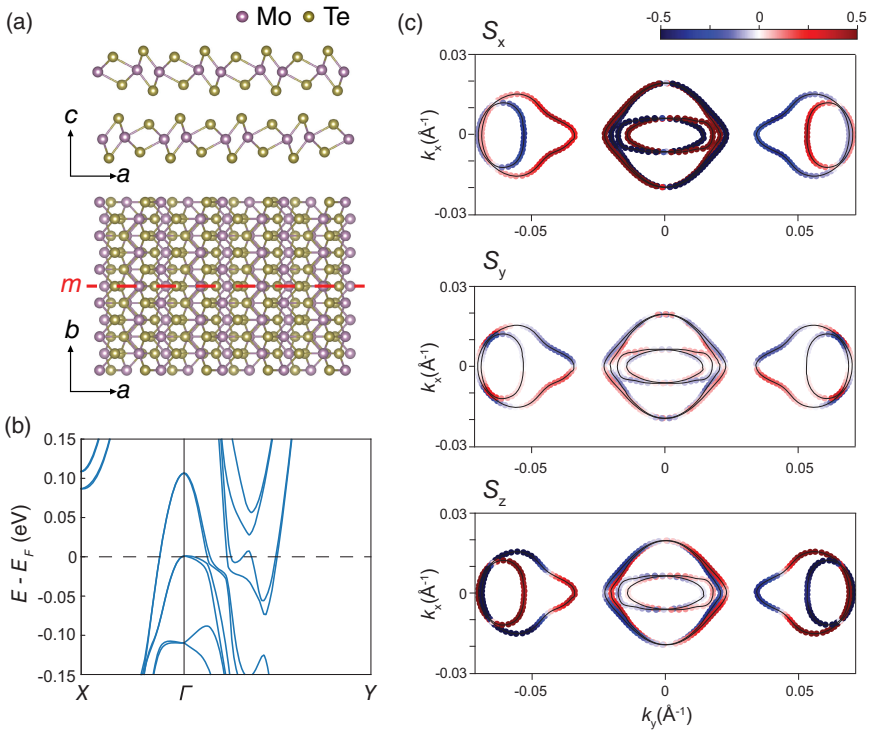

FIG. 1. (a) The side view (top) and the top view (bottom) crystal structure of bilayer $MoTe_2$. The mirror plane is labeled as the dashed red line. (b) Electronic band structure for bilayer $MoTe_2$ calculated by DFT with spin-orbit coupling included. (c) Spin texture projection for bilayer $MoTe_2$ close to the Fermi level with $E = E_F - 0.01$ eV for the S_x, S_y, and S_z components.

applied in-plane magnetic and out-of-plane electric fields through precise alignment of bilayer T_d-$MoTe_2$ using a unique two-axis, piezo rotator and spring combination.

Bilayer T_d-$MoTe_2$ has a noncentrosymmetric, orthorhombic crystal structure with Mo chains along the b axis and a mirror plane symmetry along the a and c axes, as shown in Fig. 1(a). As a result of the mirror symmetry, significant SOC is expected with a twofold rotational symmetry along the in-plane direction. From the density functional theory (DFT) calculated electronic band structure [Fig. 1(b)], we observe two spin-split electronlike bands and two spin-split holelike bands crossing the Fermi level, with the hole bands centered around the Γ point. Consistent with both monolayer and bulk $MoTe_2$, the DFT-calculated carrier density indicates a nearly perfectly compensated semimetal with hole (n_h) and electron (n_e) densities equal to $\sim 2.2 \times 10^{13}$ cm^{-2} at the Fermi level. These values are in good agreement with the carrier densities ($n_e = 2.2 \times 10^{13}$ cm^{-2}, $n_h = 2.6 \times 10^{13}$ cm^{-2} without gating) extracted from Hall measurements using a two-band semiclassical model [19]. The combination of broken inversion symmetry and large SOC gives rise to two distinct spin textures in the bilayer [see Fig. 1(c)]. For the hole pocket centered at Γ, the spin texture is nontrivial with low SOC strength and oscillates in and out of plane along k_x and k_y. For the electron pockets flanking Γ (akin to the ±Q pockets for monolayer $MoTe_2$ [8]), the spin texture has large SOC strength and resides primarily out of plane. Given the mirror-plane symmetry, anisotropic spin textures calculated by DFT, and prior models comparing different directions of the in-plane spin susceptibility [7], we expect that bilayer $MoTe_2$ will exhibit anisotropic superconducting properties under varying in-plane and out-of-plane magnetic field angles.

To systematically study the effects of the spin texture on the superconducting state, we fabricated a dual-gated heterostructure of bilayer T_d-$MoTe_2$ encapsulated in hexagonal boron nitride (hBN), allowing for continuous tuning of doping and out-of-plane electric field (see Supplemental Material [20] for details). Due to the large magnetoresistance [35] for out-of-plane magnetic fields, the possible tilted Ising superconductivity [7,8] in $MoTe_2$, and the cusplike nature of critical fields (from in to out of plane) for 2D SCs [36,37], small cants away from parallel in-plane field directions can lead to large changes in the sample resistance and obfuscate the intrinsic in-plane rotational symmetry [18,38]. To ensure that we are perfectly aligned in plane, we use a two-axis rotator stage [Fig. 2(a)]. The rotation angle of the sample along the polar direction, θ, is controlled by a spring rotator, while the azimuthal angle, ϕ, is controlled by a full 360° piezo rotator. By applying voltage to the top (V_{tg}) and bottom gates (V_{bg}) we can simultaneously and independently control the carrier density and applied displacement field, D. Because $MoTe_2$ is

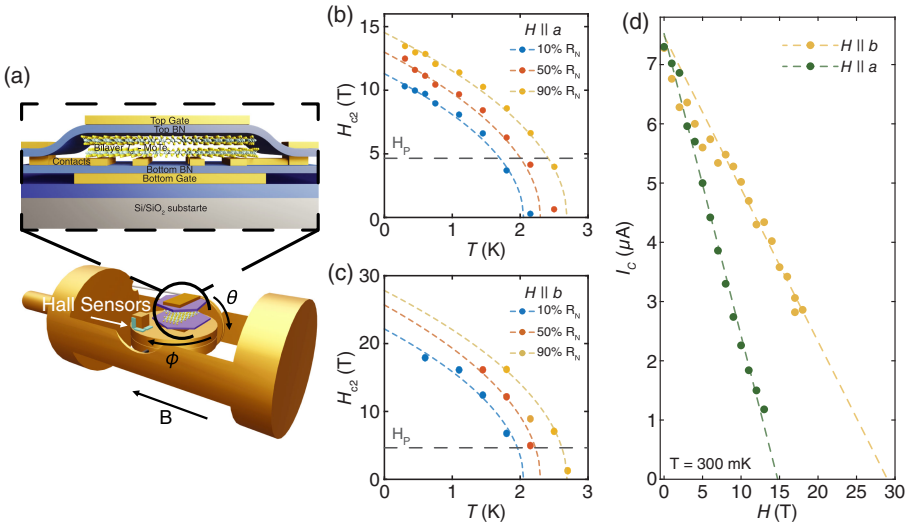

FIG. 2. (a) Schematic for the two-axis rotator stage and bilayer T_d-$MoTe_2$ device heterostructure. (b),(c) H_{c2} versus T for magnetic fields parallel to the a (b) and b (c) axes. Blue, orange, and yellow dots denote experimental H_{c2} values extracted at 10%, 50%, and 90%R_N, respectively. Dashed lines are fittings. (d) Magnetic field dependence of the critical current for fields parallel to the a and b axes.

semimetallic, we indicate changes to the carrier density as Δn, rather than an absolute density. Details for the calculated values of Δn and D are outlined in Supplemental Material [20]. For all measurements, current is passed along the b axis, which we identify as the long axis of a cleaved flake [39]. Using this setup, we first measure the in-plane upper critical fields along the a and b axes, H^a_{c2} and H^b_{c2}, respectively [Figs. 2(b) and 2(c)]. As expected, we observe a clear difference in the maximum H_{c2} between the two crystallographic directions due to the anisotropic behavior of $MoTe_2$ when fields are aligned in plane [7]. We analyze the overall trend along each direction using the thin film pair-breaking equation [2,36]

$$\ln\left(\frac{T_c}{T_{c0}}\right) + \psi\left(\frac{1}{2} + \frac{\mu_B H_\parallel^2/H_p}{2\pi k_B T_c}\right) - \psi\left(\frac{1}{2}\right) = 0,$$

where $\psi(x)$ is the digamma function, k_B is the Boltzmann constant, and μ_B is the Bohr magneton, from which we can estimate $H^a_{c2}(0)$ and $H^b_{c2}(0)$. Together, $\mu_B H^2_\parallel/H_p$ represents the effective pair-breaking energy for the superconductor, equivalent to an effective Zeeman energy brought about by spin splitting [40,41]. Near T_{c0}, this equation can be reduced to $H_{c2} = \sqrt{H_{so}H_p(1 - T_c/T_{c0})}$, where H_{so} represents an effective out-of-plane magnetic field as a result of the SOC. Using this reduced equation and keeping H_{so} as a free parameter, we fit the temperature-dependent H_{c2} data for fields along both the a and b axes [Figs. 2(b) and 2(c)]. By extrapolating using H_{c2} values at 50% of the zero-field normal state resistance (R_N), we find $H^{\parallel a}_{c2}(0)$ and $H^{\parallel b}_{c2}(0)$ are equal to 13 T and 25.7 T, respectively. To further verify the accuracy of these fittings, we also measured critical current (I_c) as a function of in-plane magnetic field. As shown in Fig. 2(d), we observe a linear dependence for both axes, in agreement with the expectations of mean-field theory [42]. The zero-temperature upper critical fields extracted from the I_c data are $H^{\parallel b}_{c2}(0) = 28.9$ T, $H^{\parallel a}_{c2}(0) = 14.7$ T, consistent with the values extracted from the temperature-dependent critical field data. We note that the anisotropy of the superconducting behavior persists for I_c, suggesting an anisotropic response of the superconducting gap with in-plane magnetic field, similar to 2M-WS_2 [11].

Both $H^{\parallel a}_{c2}(0\text{ K})$ and $H^{\parallel b}_{c2}(0\text{ K})$ are well above the Pauli limit ($H_p = 1.84T_c = 4.6$ T), with $H^{\parallel a}_{c2}(0\text{ K}) = 2.9H_p$ and $H^{\parallel b}_{c2}(0\text{ K}) = 5.6H_p$. The amount to which $H^{\parallel b}_{c2}(0\text{ K})$ exceeds the Pauli limit in bilayer $MoTe_2$ is far beyond the values observed in exfoliated monolayers ($1.9H_p$) [8] and chemical vapor deposition (CVD) grown few-layer flakes ($2.8H_p$) of $MoTe_2$. The anisotropy between the a and b axes [$H^{\parallel b}_{c2}(0\text{ K})/H^{\parallel a}_{c2}(0\text{ K})$] is 1.98, a substantial increase as compared to few-layer, CVD-grown $MoTe_2$ (1.53) [7], and bulk single crystals (1.2) [43]. Given this large anisotropy and the additional observation of Shubnikov–de Haas oscillations in the normal state [19], it is unlikely that the enhancement in H_{c2} is the result of spin-orbit scattering [44]. In previous reports [7,8], the enhanced $H^{\parallel}_{c2}$ combined with the in-plane anisotropy in few-layer $MoTe_2$ was initially considered to result from strong SOC combined with a complex spin texture inherent to the broken inversion symmetry. In this scenario, the majority of spin was considered to be locked along the $x - z$ plane, leading to enhanced upper critical fields along the y direction. As stated earlier, SOPC has also been suggested as the mechanism for enhancing $H^{\parallel}_{c2}$ in $MoTe_2$. When combined

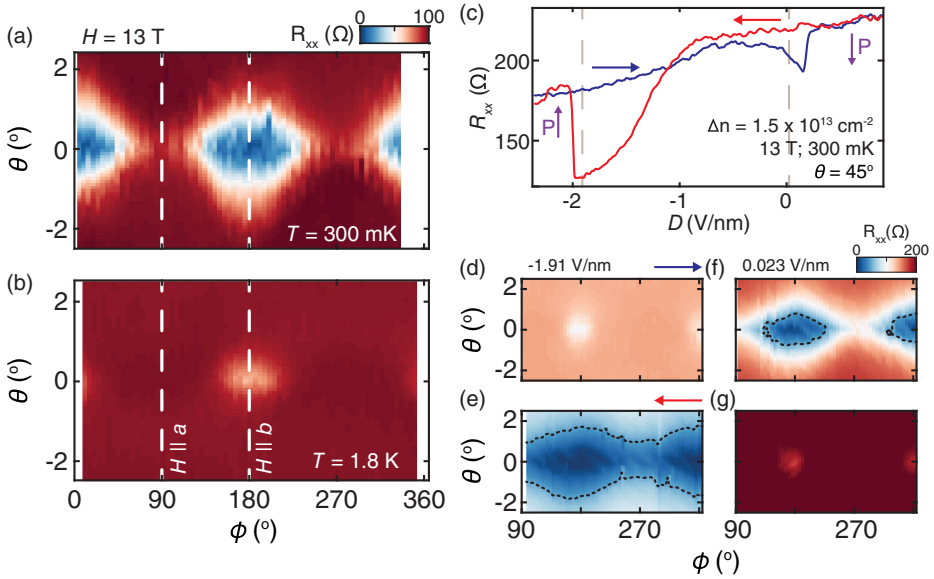

FIG. 3. In-plane symmetry and ferroelectricity. (a),(b) Mapping of rotation angle dependent resistance at 300 mK, 13 T (a) and 1.8 K, 13 T (b), indicating a twofold anisotropy within the whole superconducting range. Dashed white lines denote the positions for magnetic field parallel to the a and b axes. (c) Ferroelectric switching of bilayer $MoTe_2$ with varying displacement field, D. The internal polarization is marked with purple arrows. Red and blue arrows indicate the sweeping directions for D. (d)–(g), Evolution of superconductivity with varying D along the ferroelectric hysteresis loop for $T = 300$ mK and $B = 13$ T. The chosen values of D are indicated in (c) with dashed lines. The dashed black lines in (e),(f) denote the superconducting regions for the $50\%R_N$ criteria.

with disorder, SOPC predicts $H_{c2}^{\parallel}$'s of up to $4H_p$ along the b axis with anisotropic in-plane behavior and no SOPC enhancement of the upper critical field along the a axis [10].

Since SOPC can influence superconductivity in both centro- and noncentrosymmetric superconductors, recent works have ruled out Ising-type mechanisms by focusing on centrosymmetric 1T′ and 2M superconductors. The symmetry of multilayer $MoTe_2$ can be difficult to determine, as Raman studies have shown that both the T_d (noncentrosymmetric) and 1T′ (centrosymmetric) structures can exist at low temperature [45]. In addition, transmission electron microscopy studies have shown significant interlayer stacking disorder for bulk and few-layer mechanically exfoliated flakes [46]. Prior results also found that $H_{c2}^{\parallel}$ for the b axis remains below $4H_p$ with no other evidence for broken inversion symmetry beyond the enhanced $H_{c2}^{\parallel}$ in few-layer $MoTe_2$ and so could not rule out SOPC [7,8]. For bilayer $MoTe_2$, due to the flipped orientation between the two layers, both T_d and 1T′ and any stacking disorder via shear between layers will still break inversion symmetry, allowing tilted Ising SOC to contribute to the enhanced in-plane upper critical fields. In transport, the broken inversion symmetry of bilayer $MoTe_2$ is evidenced by the existence of a ferroelectric transition [19].

In contrast to prior works, in our bilayer $MoTe_2$ devices $H_{c2}^{\parallel}$ along the b axis far exceeds $4H_p$. For the a axis, $H_{c2}^{\parallel}$ significantly surpasses $1.2H_p$ (the maximum calculated value in the clean limit for SOPC). In combination with the anisotropy, our data is in strong agreement with the tilted Ising SOC model with spins locked along the $x-z$ plane. To further confirm this, we extract the effective SOC strength (Δ_{so}) from the pair-breaking equation, giving values of $2\Delta_{so}^{\parallel b} = 16.4$ meV for the b axis and $2\Delta_{so}^{\parallel a} = 4.3$ meV for the a axis. These values are in general agreement for the expected spin splitting of the conduction band near the Fermi level [Fig. 1(b)]. Altogether, these results suggest that tilted Ising SOC is the dominant mechanism for the observed enhanced and anisotropic upper critical fields.

To further explore the in-plane symmetry of the superconducting behavior in bilayer $MoTe_2$, we perform magnetotransport measurements while simultaneously rotating the field in (θ) and out of plane (ϕ). In Fig. 3, we map R_{xx} as a function of both θ and ϕ with the backlash from the string rotator subtracted out (see Supplemental Material [20]). Here, $\theta = 0°$ represents complete in-plane alignment and $\phi = 0°$ and 90° represent fields aligned along the b and a axes, respectively. As shown in Fig. 3(a), we begin by mapping the anisotropy of $H_{c2}^{\parallel}$ at 300 mK with a constant applied magnetic field of 13 T, close to the value of $H_{c2}^{\parallel a}(0\ \mathrm{K})$. We observe a clear twofold rotational symmetry for fields along the in-plane direction, where superconductivity persists for fields aligned along the b axis and the normal state resistance is reached for fields along the a axis. We note that there is no anisotropy for in-plane field

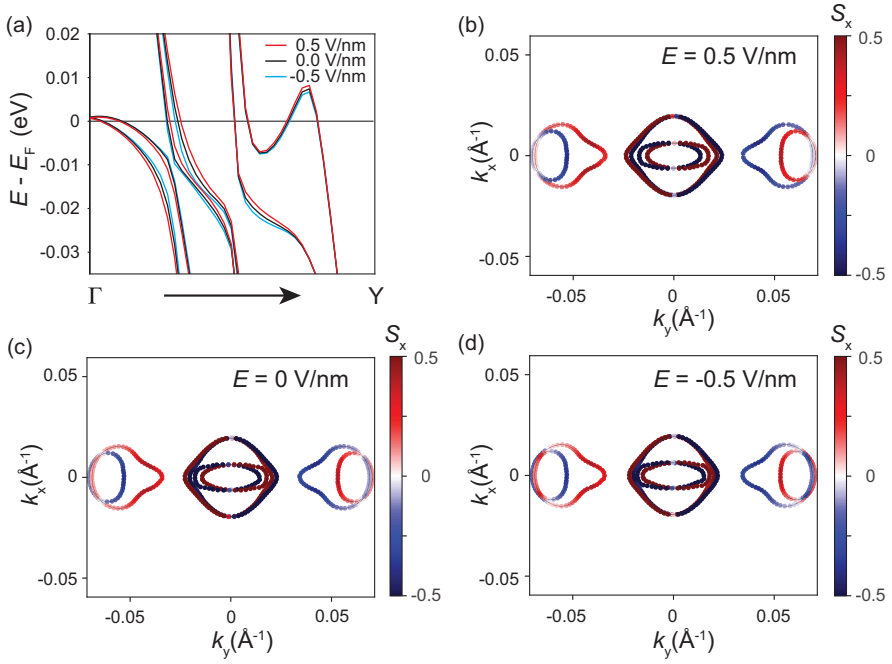

FIG. 4. (a) Electronic band structure of bilayer $MoTe_2$ under varying out-of-plane electric field. (b)–(d) Spin texture projection of bilayer $MoTe_2$ at the Fermi level for S_x component under the out-of-plane electric field of $E_z = 0.5, 0, -0.5$ V/nm, respectively.

directions observed in the normal state magnetoresistance ($\theta > 2.5°$), indicating that this effect is intrinsic to the superconducting state. This twofold rotational symmetry is consistent across bilayer samples (see Supplemental Material [20]) and does not change for all measured temperatures up to 1.8 K [$T/T_{c0} = 0.7$, Fig. 3(b)]. These results are contrary to those that have been seen in other 2D superconductors, like $NbSe_2$, where twofold and sixfold rotational symmetries depend on temperature and field. The former has been suggested as being due to s-wave and d-wave pair mixing, enabled by strain [38,47], and the latter by a transition to a FFLO state [18].

Given our recent report of ferroelectric behavior coupled to superconductivity [19], it is natural to wonder whether there could be any changes to the twofold rotational symmetry as bilayer $MoTe_2$ transitions from a ferroelectric to a paraelectric state along the interlayer sliding pathway [48,49]. In Fig. 3(c), we confirm a ferroelectric response with respect to displacement field (D). Superconductivity maximizes just before the switching of polarization, consistent with our earlier report [19]. Here, we have chosen to dope the sample with $\Delta n = 1.5 \times 10^{13}$ cm^{-2} electrons to maximize the hysteretic behavior. As shown in Figs. 3(d)–3(f), we perform the same mapping of R_{xx} versus θ and ϕ with field and temperature identical to that of Fig. 3(a) but with D set to values before and after the switching of polarization for forward and reverse directions. To ensure that we have completely switched to the "up" polarization state, we first bias the device with $D = -2.32$ V/nm and then proceed to map R_{xx} versus θ and ϕ before and after switching to the "down" polarization state for the same two values of D, -1.91 V/nm and 0.023 V/nm. We choose these values due to their close proximity to the voltages required for switching the internal polarization and the voltages required for maximizing T_c [-1.19 V/nm for "down" and 0.023 V/nm for "up"; see the dashed lines in Fig. 3(c)]. We observe clear hysteretic behavior in these maps, reflected by the changing R_N and H_{c2} for the same values of D. However, much like in the $D = 0$ V/nm case discussed earlier, we observe the same twofold rotational symmetry for the superconducting state. From these results, and combined with the fact that we observe ferroelectric behavior, we can conclude that inversion symmetry is broken in bilayer $MoTe_2$, as expected from the crystal structure, and that this broken inversion symmetry combined with the mirror symmetry along the $b-c$ plane, imparts a complex spin texture that is responsible for the observed anisotropy in $H_{c2}^{\parallel}$. These results are in agreement with our earlier reports on monolayer $MoTe_2$ where, under the assumption of broken inversion symmetry, the tilted spin texture gives rise to a twofold rotational symmetry for H_{c2} [8]. From the calculated spin texture in Fig. 1, we can average across the Fermi surface for S_x, S_y, and S_z components and find that the average value of S_x is greater than that of S_y. Like in the case of type-I Ising SOC, the tilting given by the finite S_x value for individual electron pockets will impart a resistance for spins to align away from the x-direction. As a result, $H_{c2}^{\parallel}$ will maximize perpendicular to the a axis (i.e, $H \| b$), in agreement with our observations. The

origins of this difference in spin textures between S_x and S_y can be traced back to the breaking of the out-of-plane mirror symmetry given by the bilayer crystal structure. [7].

The lack of change to the rotational symmetry of the superconducting gap for in-plane magnetic fields through the ferroelectric transition pathway is not surprising. The moderate carrier densities of bilayer $MoTe_2$ significantly screen out-of-plane electric fields and, as a result, minimize any additional contribution to Rashba spin-orbit coupling. To see this more clearly, in Fig. 4(a) we compare the DFT-calculated electronic band structure for applied out-of-plane electric fields (−0.5, 0.0, and 0.5 V/nm). While there is a minor shift in the energy of the bands (up to 2 meV), there is no appreciable change in the spin splitting between spin-split conduction and valence bands near E_F. As expected, when reexamining the Fermi surfaces and concomitant spin textures as a function of applied out-of-plane electric fields, there is no change in the symmetry of the spin texture, nor is there any discernible change in the size of the Fermi pockets and maximum values of S_x, S_y, and S_z for the range of out-of-plane electric fields that we have calculated. One caveat to this interpretation may be the existence of a paraelectric phase along the ferroelectric transition pathway, which has been suggested for bilayer WTe_2 [48,49] (isostructural to bilayer $MoTe_2$). Assuming this paraelectric structure, we again calculate the electronic band structure and spin texture (see Supplemental Material [20]). While we find little change in the electronic band structure from that of the polar one, the magnitudes of S_x and S_y significantly decrease for the electron pockets, while remaining similar for the hole pockets. This suggests that if any intermediate metastable paraelectric phase existed along the transition pathway, we should observe the emergence of an isotropic superconducting gap. However, as pointed out in Figs. 3(d)–3(g), we observe no collapse of the anisotropy for any value of the displacement field. This suggests that domains of internal polarization may be remaining as "up" or "down" until sufficient displacement field of opposite sign is reached and the entire domain flips at once, instead of passing through an intermediate nonpolar structure. However, more work is necessary to determine the true nature of the ferroelectric transition pathway.

In summary, we observe a robust twofold anisotropic superconducting behavior in bilayer T_d-$MoTe_2$, where the upper critical field maximizes and minimizes with respect to the in-plane crystal symmetry. This twofold rotational symmetry of the superconducting gap persists for all values of temperature, parallel magnetic field, applied displacement field, carrier doping, and internal polarization switching within the superconducting regime. The lack of a change in the rotational symmetry agrees with the calculated electronic band structures under electric field for the polar structure. While our evidence strongly suggests that tilted Ising SOC is responsible for the twofold rotational symmetry, we note that it is not well understood whether other competing mechanisms can coexist to enhance the upper critical along the same axes (e.g., SOPC combined with tilted Ising SOC). Future work on other centro- and noncentrosymmetric layer numbers of T_d-$MoTe_2$ may elucidate more on these effects. We also note that in our earlier work we observed large changes in H_{c2} and T_c throughout the ferroelectric hysteresis loop, which we surmised were the result of an increase in Fermi surface nesting as the hole pocket massively increases in size while the bilayer transitions through the loop [19]. While measurements of the carrier density indicate that this interpretation may still be correct, our calculations presented in this Letter show that electric fields alone cannot cause such a change to the size of the hole pockets.

Acknowledgments—We thank Rafael M. Fernandes and Alex Levchenko for fruitful discussions. This work was supported by the Department of Energy Office of Basic Energy Sciences (DE-SC0023866), including theory (X. Q. and A. S.), measurements (D. R. and Z. L.), and analysis (Z. L., D. R., A. S., and X. Q.), and by the NSF MRSEC program through Columbia University in the Center for Precision-Assembled Quantum Materials (DMR-2011738) (A. J., C. R. D., and A. P. N.). W. Z. and L. B. were supported by the NSF Division of Materials Research (DMR-2219003). Growth of *h*-BN crystals was supported by the Elemental Strategy Initiative conducted by the MEXT, Japan (Grant No. JPMXP0112101001), JSPS KAKENHI (Grant Nos. 19H05790, 20H00354 and 21H05233), and A3 Foresight by JSPS (T. T. and K. W.). Growth of $MoTe_2$ single crystals was supported by the Wisconsin Alumni Research Foundation (Y. H.). A portion of this work was performed at the National High Magnetic Field Laboratory, which is supported by the NSF Cooperative Agreement No. DMR-2128556 and the State of Florida. Portions of this research were conducted with the advanced computing resources provided by Texas A&M High Performance Research Computing. The authors gratefully acknowledge the use of facilities and instrumentation in the Wisconsin Center for Nanoscale Technology. This center is partially supported by the Wisconsin Materials Research Science and Engineering Center (NSF DMR-2309000) and by the University of Wisconsin–Madison.

[1] J. Lu, O. Zheliuk, I. Leermakers, N. F. Yuan, U. Zeitler, K. T. Law, and J. Ye, Science **350**, 1353 (2015).
[2] X. Xi, Z. Wang, W. Zhao, J.-H. Park, K. T. Law, H. Berger, L. Forró, J. Shan, and K. F. Mak, Nat. Phys. **12**, 139 (2016).
[3] S. C. De la Barrera, M. R. Sinko, D. P. Gopalan, N. Sivadas, K. L. Seyler, K. Watanabe, T. Taniguchi, A. W. Tsen, X. Xu, D. Xiao, and B. M. Hunt, Nat. Commun. **9**, 1427 (2018).
[4] C. Wang, B. Lian, X. Guo, J. Mao, Z. Zhang, D. Zhang, B.-L. Gu, Y. Xu, and W. Duan, Phys. Rev. Lett. **123**, 126402 (2019).

[5] J. Falson, Y. Xu, M. Liao, Y. Zang, K. Zhu, C. Wang, Z. Zhang, H. Liu, W. Duan, K. He, H. Liu, J. H. Smet, D. Zhang, and Q.-K. Xue, Science **367**, 1454 (2020).

[6] Y. Liu, Y. Xu, J. Sun, C. Liu, Y. Liu, C. Wang, Z. Zhang, K. Gu, Y. Tang, C. Ding, H. Liu, H. Yao, X. Lin, L. Wang, Q.-K. Xue, and J. Wang, Nano Lett. **20**, 5728 (2020).

[7] J. Cui, P. Li, J. Zhou, W.-Y. He, X. Huang, J. Yi, J. Fan, Z. Ji, X. Jing, F. Qu, Z. G. Cheng, C. Yang, L. Lu, K. Suenaga, J. Liu, K. T. Law, J. Lin, Z. Liu, and G. Liu, Nat. Commun. **10**, 2044 (2019).

[8] D. A. Rhodes, A. Jindal, N. F. Yuan, Y. Jung, A. Antony, H. Wang, B. Kim, Y.-c. Chiu, T. Taniguchi, K. Watanabe, K. Barmak, L. Balicas, C. R. Dean, X. Qian, L. Fu, A. N. Pasupathy, and J. Hone, Nano Lett. **21**, 2505 (2021).

[9] S. Yoshizawa, T. Kobayashi, Y. Nakata, K. Yaji, K. Yokota, F. Komori, S. Shin, K. Sakamoto, and T. Uchihashi, Nat. Commun. **12**, 1462 (2021).

[10] Y.-M. Xie, B. T. Zhou, and K. T. Law, Phys. Rev. Lett. **125**, 107001 (2020).

[11] E. Zhang *et al.*, Nat. Phys. **19**, 106 (2023).

[12] X. Qian, J. Liu, L. Fu, and J. Li, Science **346**, 1344 (2014).

[13] S. Tang *et al.*, Nat. Phys. **13**, 683 (2017).

[14] M. Sato and Y. Ando, Rep. Prog. Phys. **80**, 076501 (2017).

[15] J.-H. Lee and Y.-W. Son, Phys. Chem. Chem. Phys. **23**, 17279 (2021).

[16] X. Liu, Y. X. Chong, R. Sharma, and J. S. Davis, Science **372**, 1447 (2021).

[17] L.-X. Wei, P.-C. Xiao, F. Li, L. Wang, B.-Y. Deng, F.-J. Cheng, F.-W. Zheng, N. Hao, P. Zhang, X.-C. Ma, Q.-K. Xue, and C.-L. Song, arXiv:2308.11101.

[18] P. Wan, O. Zheliuk, N. F. Yuan, X. Peng, L. Zhang, M. Liang, U. Zeitler, S. Wiedmann, N. E. Hussey, T. T. Palstra, and J. Ye, Nature (London) **619**, 46 (2023).

[19] A. Jindal, A. Saha, Z. Li, T. Taniguchi, K. Watanabe, J. C. Hone, T. Birol, R. M. Fernandes, C. R. Dean, A. N. Pasupathy, and D. A. Rhodes, Nature (London) **613**, 48 (2023).

[20] See Supplemental Material at http://link.aps.org/supplemental/10.1103/PhysRevLett.133.216002 for descriptions of materials synthesis, heterostructure fabrication, experimental setup, measurements, and theoretical calculations, which includes Refs. [21–34].

[21] L. Wang, I. Meric, P. Huang, Q. Gao, Y. Gao, H. Tran, T. Taniguchi, K. Watanabe, L. Campos, D. Muller, J. Guo, P. Kim, J. Hone, K. Shepard, and C. Dean, Science **342**, 614 (2013).

[22] J. J. Schwartz, H.-J. Chuang, M. R. Rosenberger, S. V. Sivaram, K. M. McCreary, B. T. Jonker, and A. Centrone, ACS Appl. Mater. Interfaces **11**, 25578 (2019).

[23] V. Fatemi, S. Wu, Y. Cao, L. Bretheau, Q. D. Gibson, K. Watanabe, T. Taniguchi, R. J. Cava, and P. Jarillo-Herrero, Science **362**, 926 (2018).

[24] M. Yankowitz, S. Chen, H. Polshyn, Y. Zhang, K. Watanabe, T. Taniguchi, D. Graf, A. F. Young, and C. R. Dean, Science **363**, 1059 (2019).

[25] P. Hohenberg and W. Kohn, Phys. Rev. **136**, B864 (1964).

[26] W. Kohn and L. J. Sham, Phys. Rev. **140**, A1133 (1965).

[27] G. Kresse and J. Furthmüller, Phys. Rev. B **54**, 11169 (1996).

[28] G. Kresse and J. Furthmüller, Comput. Mater. Sci. **6**, 15 (1996).

[29] P. E. Blöchl, Phys. Rev. B **50**, 17953 (1994).

[30] J. P. Perdew, K. Burke, and M. Ernzerhof, Phys. Rev. Lett. **77**, 3865 (1996).

[31] S. P. Ong, W. D. Richards, A. Jain, G. Hautier, M. Kocher, S. Cholia, D. Gunter, V. L. Chevrier, K. A. Persson, and G. Ceder, Comput. Mater. Sci. **68**, 314 (2013).

[32] U. Herath, P. Tavadze, X. He, E. Bousquet, S. Singh, F. Muñoz, and A. H. Romero, Comput. Phys. Commun. **251**, 107080 (2020).

[33] L. Lang, P. Tavadze, A. Tellez, E. Bousquet, H. Xu, F. Muñoz, N. Vasquez, U. Herath, and A. H. Romero, Comput. Phys. Commun. **297**, 109063 (2024).

[34] T. Fukui and Y. Hatsugai, J. Phys. Soc. Jpn. **76**, 053702 (2007).

[35] F. C. Chen, H. Y. Lv, X. Luo, W. J. Lu, Q. L. Pei, G. T. Lin, Y. Y. Han, X. B. Zhu, W. H. Song, and Y. P. Sun, Phys. Rev. B **94**, 235154 (2016).

[36] M. Tinkham, *Introduction to Superconductivity* (Dover Publications, Inc., Mineola, New York, 2004).

[37] Y. Saito, T. Nojima, and Y. Iwasa, Nat. Rev. Mater. **2**, 16094 (2016).

[38] A. Hamill, B. Heischmidt, E. Sohn, D. Shaffer, K.-T. Tsai, X. Zhang, X. Xi, A. Suslov, H. Berger, L. Forró, F. J. Burnell, J. Shan, K. F. Mak, R. M. Fernandes, K. Wang, and V. S. Pribiag, Nat. Phys. **17**, 949 (2021).

[39] R. Beams, L. G. Cançado, S. Krylyuk, I. Kalish, B. Kalanyan, A. K. Singh, K. Choudhary, A. Bruma, P. M. Vora, F. Tavazza, A. V. Davydov, and S. J. Stranick, ACS Nano **10**, 9626 (2016).

[40] M. Sigrist, AIP Conf. Proc. **1162**, 55 (2009).

[41] S. J. Youn, M. H. Fischer, S. H. Rhim, M. Sigrist, and D. F. Agterberg, Phys. Rev. B **85**, 220505(R) (2012).

[42] V. M. Galitski and A. I. Larkin, Phys. Rev. Lett. **87**, 087001 (2001).

[43] D. Rhodes, R. Schönemann, N. Aryal, Q. Zhou, Q. Zhang, E. Kampert, Y.-C. Chiu, Y. Lai, Y. Shimura, G. McCandless, J. Chan, D. Paley, L. J, A. Finke, J. Ruff, S. Das, E. Manousakis, and L. Balicas, Phys. Rev. B **96**, 165134 (2017).

[44] R. A. Klemm, A. Luther, and M. Beasley, Phys. Rev. B **12**, 877 (1975).

[45] Y. Cheon, S. Y. Lim, K. Kim, and H. Cheong, ACS Nano **15**, 2962 (2021).

[46] J. L. Hart, L. Bhatt, Y. Zhu, M.-G. Han, E. Bianco, S. Li, D. J. Hynek, J. A. Schneeloch, Y. Tao, D. Louca, P. Guo, Y. Zhu, F. Jornada, E. J. Reed, L. F. Kourkoutis, and J. J. Cha, Nat. Commun. **14**, 4803 (2023).

[47] M. Haim, A. Levchenko, and M. Khodas, Phys. Rev. B **105**, 024515 (2022).

[48] Q. Yang, M. Wu, and J. Li, J. Phys. Chem. Lett. **9**, 7160 (2018).

[49] X. Liu, Y. Yang, T. Hu, G. Zhao, C. Chen, and W. Ren, Nanoscale **11**, 18575 (2019).